Applied Catalysis B: Environmental 170-171 (2015) 17–24

Contents lists available at ScienceDirect

Applied Catalysis B: Environmental

journal homepage: www.elsevier.com/locate/apcatb

N-doped $Na_2Ti_6O_{13}$@TiO_2 core–shell nanobelts with exposed {1 0 1} anatase facets and enhanced visible light photocatalytic performance

Chao Liu[a], Tao Sun[a], Liang Wu[a], Jiyuan Liang[a], Qianjin Huang[b], Jing Chen[b], Wenhua Hou[a,*]

[a] Key Laboratory of Mesoscopic Chemistry of MOE, School of Chemistry and Chemical Engineering, Nanjing University, Nanjing 210093, PR China
[b] Department of Applied Chemistry, College of Science, Nanjing University of Technology, Nanjing 210009, PR China

ARTICLE INFO

Article history:
Received 10 November 2014
Received in revised form 13 January 2015
Accepted 16 January 2015
Available online 21 January 2015

Keywords:
Titanate
Anatase
Core–shell
Doping
Photodegradation

ABSTRACT

N-doped $Na_2Ti_6O_{13}$@TiO_2 core–shell nanobelts have been successfully synthesized by first mixing $Na_2Ti_3O_7$ with titanium isopropoxide, and then calcinating with urea in air. A structural evolution from the phase $Na_2Ti_3O_7$ to $Na_2Ti_6O_{13}$ occurred as the TiO_6 octahedra in $Na_2Ti_6O_{13}$ is more regular. Anatase TiO_2 nanoparticles (NPs) with specifically exposed {1 0 1} facets were deposited on the external surface of $Na_2Ti_6O_{13}$ nanobelts, forming the closely contacted interface between two components due to the common structural features of TiO_6 octahedra in anatase TiO_2 and $Na_2Ti_6O_{13}$. The reductive {1 0 1} facets could be acted as a possible reservoir of the photogenerated electrons, yielding a highly reactive surface for the reduction of O_2–$O_2^{\bullet-}$ and thus, lowering the recombination rate of photogenerated electron–hole pairs. The anisotropically shaped titanate nanobelts in the obtained composites possessed a higher charge carrier mobility and provided the pathway for quick transport of charge carriers throughout the longitudinal direction to different reaction sites for subsequent reactions. The doped N atoms were mainly located in the crystal lattices of TiO_2, giving rise to the visible light response. Owing to the combined effects of hybridization, morphology engineering, and N doping, the obtained composite showed a high stability and an enhanced catalytic activity for the photodegradation of methylene blue (MB) solution under visible light irradiation. In addition, it was found that both an appropriate mass ratio of TiO_2 to titanate and a suitable content of doped N were essential for achieving an excellent performance. The present work may provide an insight for the fabrication of delicate composite photocatalysts with a high performance.

© 2015 Elsevier B.V. All rights reserved.

1. Introduction

Photocatalysis, using semiconductors, has become an area of great research interest due to its potential applications in solving energy supply and environmental pollution problems [1–5]. TiO_2 is the most widely investigated photocatalyst due to its high photoactivity, exceptional optical and electronic properties, low cost and toxicity, and good chemical and thermal stability [6,7]. However, its practical applications are greatly restricted due to the narrow light-response range and low separation probability of the photoinduced electron–hole pairs. Thus, much effort has been devoted to exploit new visible light-driven photocatalysts [8].

Alkali metal titanates, with the general formula of $A_2Ti_nO_{2n+1}$ (A = Li, Na, and K and n = 3–8), have an open-layered structure (n = 2–4) or a tunnel structure (n = 6–8) depending on the value of n. For example, $Na_2Ti_3O_7$ with three TiO_6 octahedra in a unit cell has a layered structure while $Na_2Ti_6O_{13}$ with six TiO_6 octahedra in a unit cell has a tunnel structure. Due to their stoichiometry-dependent structure and physicochemical properties, alkali metal titanates have been intensively explored in such applications as photocatalyst [9–11], lithium and sodium ion battery [12,13], gas and humidity sensing, and antibacterial agent [14,15]. As photocatalysts, these structures are suitable both for the accommodation of catalytic active phase (e.g., metal oxides) to raise the separation efficiency of photo-excited charge carriers and for the transfer of these carriers to adsorbed reactants at the surface [16]. However, $Na_2Ti_6O_{13}$ itself has a relatively wide band gap and is thus, active only under UV light. Since UV light only accounts for 4% of the solar energy spectrum while visible light occupies 46% of the spectrum, it is of a great significance to design a visible light-responsive $Na_2Ti_6O_{13}$ photocatalyst.

* Corresponding author. Tel.: +86 25 83686001.
E-mail address: whou@nju.edu.cn (W. Hou).

http://dx.doi.org/10.1016/j.apcatb.2015.01.026
0926-3373/© 2015 Elsevier B.V. All rights reserved.

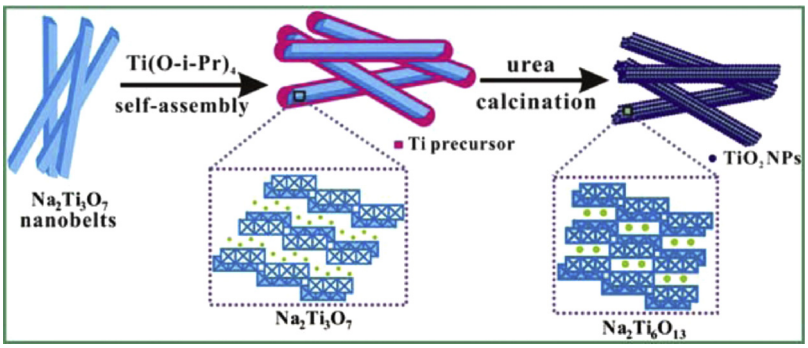

Fig. 1. A schematic illustration for the synthesis of N-doped $Na_2Ti_6O_{13}$@TiO_2 core–shell nanobelts.

To efficiently utilize solar energy, many strategies including non-metal doping, hybridization, and morphology engineering have been employed [17–21]. The non-metal doping will improve the visible-light-driven photocatalytic activity due to the band gap narrowing, resulting from the creation of doping energy levels above the VB [22,23]. On the other hand, it was demonstrated that the hybridization of different semiconductors to form a heterojunction structure could greatly decrease the recombination probability of photogenerated electron–hole pairs and thus, increase the lifetime of charge carries, giving rise to an increased activity [24–26]. In addition, the morphology engineering of TiO_2 to form specifically exposed crystal facets has also been proved to be effective in enhancing the photocatalytic performance, although there are some contradictory interpretations concerning how the exposed facets of anatase affect the photoactivity [27–32].

Composites containing titanate and TiO_2 have been synthesized and their higher photocatalytic activities have been demonstrated. For example, N-doped titanate–anatase core–shell nanobelts in which anatase nanorods with specifically exposed {1 0 1} facets were deposited on the external surface of $K_2Ti_4O_9$ nanobelts were reported to have an excellent photocatalytic performance in the degradation of MB [33]. Nevertheless, the complicated preparation process limited its practical application. Hydrogen titanate nanofibers covered with TiO_2 nanocrystals were also achieved through the wet chemistry reaction [34,35]. Yet the overall photocatalytic performance was restricted as most titanate surfaces were not fully used [36]. Furthermore, titanate@TiO_2 core–shell photocatalysts have been prepared with the addition of cetyl trimethylammonium bromide (CTAB), showing a higher photocatalytic activity than other samples in the degradation of benzonic acid [37]. However, the result was obtained under irradiation of UV light rather than visible light.

In this work, N-doped $Na_2Ti_6O_{13}$@TiO_2 core–shell nanobelts with exposed {1 0 1} anatase facets have been synthesized via a facile two-step route. The structure, surface morphology, and photocatalytic performance in the degradation of MB of the resultant samples have been studied and discussed in detail. The effects of loading amount of TiO_2 and content of doped N were systematically investigated. Moreover, a possible photocatalytic mechanism was proposed based on the experimental results.

2. Experiment

2.1. Catalysts preparation

Firstly, $Na_2Ti_3O_7$ was prepared by the conventional solid state reaction, according to a procedure described in the literature [38]. To prepare N-doped $Na_2Ti_6O_{13}$@TiO_2 core–shell nanobelts, the as-prepared $Na_2Ti_3O_7$ (2.0 g) was dispersed in ethanol (50 mL) by ultrasonic treatment for 10 min, followed by stirring. After 12 h, a certain volume of titanium isopropoxide (Ti(O–*i*–Pr)$_4$) was added dropwise into the above suspension under stirring. After 12 h, the resultant suspension was transferred to a petri-dish and dried at room temperature to allow solvent evaporation. After complete evaporation of ethanol, the obtained solid sample (1.0 g) was finely milled with urea, and then the mixture was calcined in air at 500 °C for 10 h with a heating rate of 2 °C/min [39]. By changing the volume (1, 3, 6, 12, and 30 mL) of Ti(O–*i*–Pr)$_4$ and the mass (0.25, 1.0, 2.0, and 3.0 g) of urea, a series of samples with different loading amounts of TiO_2 and contents of doped N were obtained. The resultant samples were denoted as N–TTO-*x*-*y*, where *x* is the volume of Ti(O–*i*–Pr)$_4$ and *y* is the mass of urea. For *x* = 1, 3, 6, 12, and 30, the corresponding loading amount of TiO_2 is 12.4, 29.8, 45.9, 63.0, and 81.0 wt%, respectively. For *y* = 0.25, 1.0, 2.0, and 3.0, the corresponding content of doped N is 0.19, 0.67, 1.41, and 2.65 at%, respectively (also see Tables S1 and S2).

For comparison, an undoped sample (denoted as TTO-6) was prepared through a similar process in which no urea was added and the volume of Ti(O–*i*–Pr)$_4$ was 6 mL. In addition, N-doped TiO_2 (denoted as N–TiO_2) was also prepared through a similar process in which no $Na_2Ti_3O_7$ was added while the volume of Ti(O–*i*–Pr)$_4$ and the mass of urea are 10 mL and 2.0 g, respectively.

A schematic illustration for the formation process of N–TTO-*x*-*y* core–shell nanobelts is presented in Fig. 1. Upon reaction with Ti(O–*i*–Pr)$_4$, $Na_2Ti_3O_7$ nanobelts were covered with Ti precursor through a self-assembly process. Then, after mixing with urea and calcination in air, N-doped $Na_2Ti_6O_{13}$@TiO_2 core–shell nanobelts in which the anatase TiO_2 NPs were deposited on the external surface of bulk titanate were obtained. In addition, a structural evolution from the phase $Na_2Ti_3O_7$ to $Na_2Ti_6O_{13}$ was fully accomplished with the help of Ti precursor.

2.2. Characterization techniques

Powder X-ray diffraction (XRD) patterns of the obtained samples were taken on a Philip-X'Pert X-ray diffractometer with a Cu Kα radiation (λ = 1.5418 Å) and Ni filter at a scanning rate of 0.2°/s in a 2θ range of 5–60°. Ultraviolet visible diffuse reflectance spectra were obtained on a UV–vis spectrophotometer (Shimadzu, UV-2401) using $BaSO_4$ as reference. The morphology was investigated by scanning electron microscopy (SEM, JEOL JEM-6300F) and transmission electron microscopy (TEM, JEOL JEM-200CX, operating at an accelerating voltage of 200 kV). For TEM observation, the sample was dispersed in ethanol by ultrasonic treatment and then dropped onto carbon-coated copper grids. X-ray photoelectron spectroscopic (XPS) analysis was carried out on an X-ray photoelectron spectrometer (Thermo Fisher Scientific, K-Alpha) equipped with a hemispherical electron analyzer (pass energy of 20 eV) and an Al Kα ($h\nu$ = 1486.6 eV) X-ray source. The binding energies (BE) were referenced to the adventitious *C* 1s peak (284.6 eV) which was used as

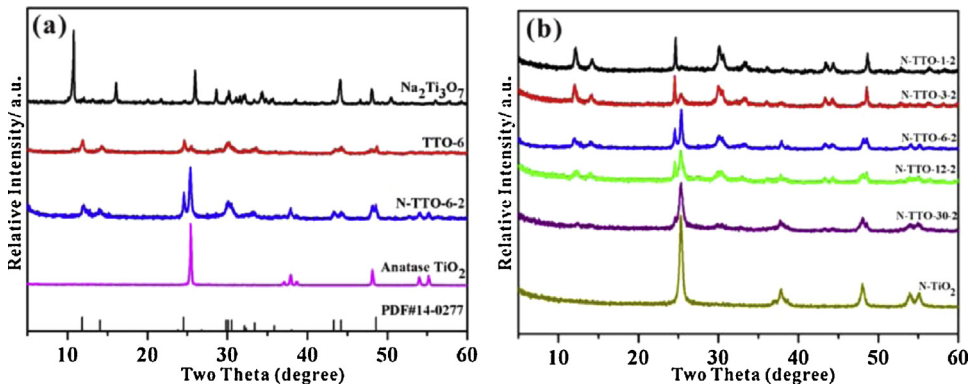

Fig. 2. XRD patterns of (a) $Na_2Ti_3O_7$, TTO-6, N–TTO-6-2 and commercial anatase TiO_2 (The standard data for monoclinic $Na_2Ti_6O_{13}$ (PDF # 14-0277) is also presented at the bottom for comparison.), and (b) N–TTO-*x*-2 series composites with different loading amounts of TiO_2 (*x* = 1, 3, 6, 12, and 30) and N–TiO_2.

an internal standard to take into account charging effects. A combination of Gaussian and Lorentzian functions was used to fit the curves. Photoluminescence (PL) spectra were recorded on a 48,000 DSCF luminescence spectrometer at room temperature by using a continuous-wave 325 nm He–Cd laser as the excitation source. The sample was pressed into a thin disk and fixed in a homemade quartz cell.

2.3. Photocatalytic reaction tests

The visible light photocatalytic activity was evaluated by the degradation of MB in aqueous solution. Firstly, 50 mg of catalyst was suspended in an MB aqueous solution (1.0×10^{-5} M) in the dark for more than 1 h in order to reach an adsorption–desorption equilibrium. After equilibrium, the catalyst was separated and re-dispersed in an aqueous solution of MB (100 mL, 1.0×10^{-5} M) in a beaker with a circulating water system to remove the thermal effect of light. Light from a 300 W Xe lamp, passed through a UV light filter film (to remove radiation with $\lambda < 420$ nm), was focused onto the reaction cell. When the light was turned on, at given time intervals, approximately 4 mL of the reaction suspension was sampled and separated by means of high-speed centrifugation. The filtrates were analyzed by recording the maximum absorbance at 664 nm in the UV–vis spectrum of MB. The degradation efficiency at time *t* was determined from the value of C_t/C_0, where C_0 is the initial concentration and C_t is the concentration of MB at time *t*.

3. Results and discussion

3.1. XRD analysis

The structure and crystallinity of the resulted samples were identified by XRD. As shown in Fig. 2(a), the XRD pattern of the as-prepared layered $Na_2Ti_3O_7$ is in good accordance with that in the literature [38], indicating the formation of pure $Na_2Ti_3O_7$ phase. After mixing with Ti(O–*i*–Pr)$_4$ and urea, the anatase TiO_2 was formed and deposited on the external surface of bulk titanate after calcination in air at 500 °C. In addition, it was found that the phase of $Na_2Ti_3O_7$ was fully disappeared and only the crystal phase of $Na_2Ti_6O_{13}$ existed, indicating that a structural evolution from the phase $Na_2Ti_3O_7$ to $Na_2Ti_6O_{13}$ was fully accomplished. Compared with the pure $Na_2Ti_3O_7$, the XRD pattern of the resulted N–TTO-6-2 showed significantly decreased and slightly broadened diffraction peaks due to the coverage of anatase TiO_2 nanoparticles on the external surface of $Na_2Ti_6O_{13}$. By comparison, the resultant TTO-6 without the addition of urea showed the similar XRD pattern with N–TTO-6-2, indicating that the addition of urea was not responsible for the structural evolution from the phase $Na_2Ti_3O_7$ to $Na_2Ti_6O_{13}$. Additionally, the XRD patterns of pure $Na_2Ti_3O_7$ after calcination in air at different temperatures for 10 h are showed in Fig. S1. Only when the calcination temperature was higher than ~950 °C, the structural evolution from the pure phase $Na_2Ti_3O_7$ to $Na_2Ti_6O_{13}$ could be observed. Thus, it can be concluded that the temperature for the structural evolution from $Na_2Ti_3O_7$ to $Na_2Ti_6O_{13}$ is greatly decreased with the help of Ti(O–*i*–Pr)$_4$.

As shown in Fig. 2(b), the diffraction peak intensities of TiO_2 are gradually increased while those of $Na_2Ti_6O_{13}$ weakened as the amount of TiO_2 is increased in the resulted N–TTO-*x*-2 series composites. It indicates that more and more surface of titanate is covered by TiO_2 and thus, a complete shell of TiO_2 is formed and its thickness is gradually increased with the loading amount of TiO_2. In addition, it can be observed that the content of doped N has no significant effect on the product structure (see Fig. S2).

As shown in Fig. 1, in the lattice of $Na_2Ti_6O_{13}$, TiO_6 octahedra share edges at one level in line group and each group is joined above and below to similar groups by further edge sharing, resulting in a zigzag ribbon structure. The zigzag ribbon structure and TiO_6 octahedra sharing four edges were also observed in the anatase lattice [40]. The common structural features of TiO_6 octahedra in anatase TiO_2 and $Na_2Ti_6O_{13}$ reveal that anatase TiO_2 can be deposited on the external surface of $Na_2Ti_6O_{13}$ to form the closely contacted interface and thus, a heterojunction. Nevertheless, being contrary to $Na_2Ti_3O_7$, there is no terminal oxygen atom in the crystal structure of $Na_2Ti_6O_{13}$ and all oxygen atoms at the surface are linearly coordinated by titanium atoms, indicating that TiO_6 octahedra in $Na_2Ti_6O_{13}$ are more regular than those in $Na_2Ti_3O_7$ [41]. Thus, a phase transition from $Na_2Ti_3O_7$ to $Na_2Ti_6O_{13}$ occurred during the preparation of N–TTO-*x*-*y* series composites.

3.2. Morphology

Fig. 3 shows EM images of $Na_2Ti_3O_7$ and N–TTO-6-2. As shown in Fig. 3(a), the as-prepared $Na_2Ti_3O_7$ consists of nanobelts with a thickness of ~200–300 nm and a length of ~1 μm. Compared with pure titanate, the hierarchical core–shell structure of N–TTO-6-2 is clearly visible and anatase TiO_2 NPs with a size of ~40 nm are densely assembled on the external surface of titanate nanobelts (Fig. 3(b)). In addition, the HRTEM image of N–TTO-6-2 also confirms that the composite material possesses a hierarchical core–shell heterostructure with the anatase phase forming the shell around titanate core (Fig. 3(c)). The shell thickness of TiO_2 is around 15–20 nm. For TiO_2 shell, the well-resolved interplanar spacing of the adjacent lattice fringes was about 0.35 nm (Fig. 3(d)). Considering the crystallographic symmetry of anatase nanoparticles, the dominant exposed facets can be identified as {1 0 1} planes. For $Na_2Ti_6O_{13}$ core (Fig. 3(e)), the clear lattice fringe confirms the

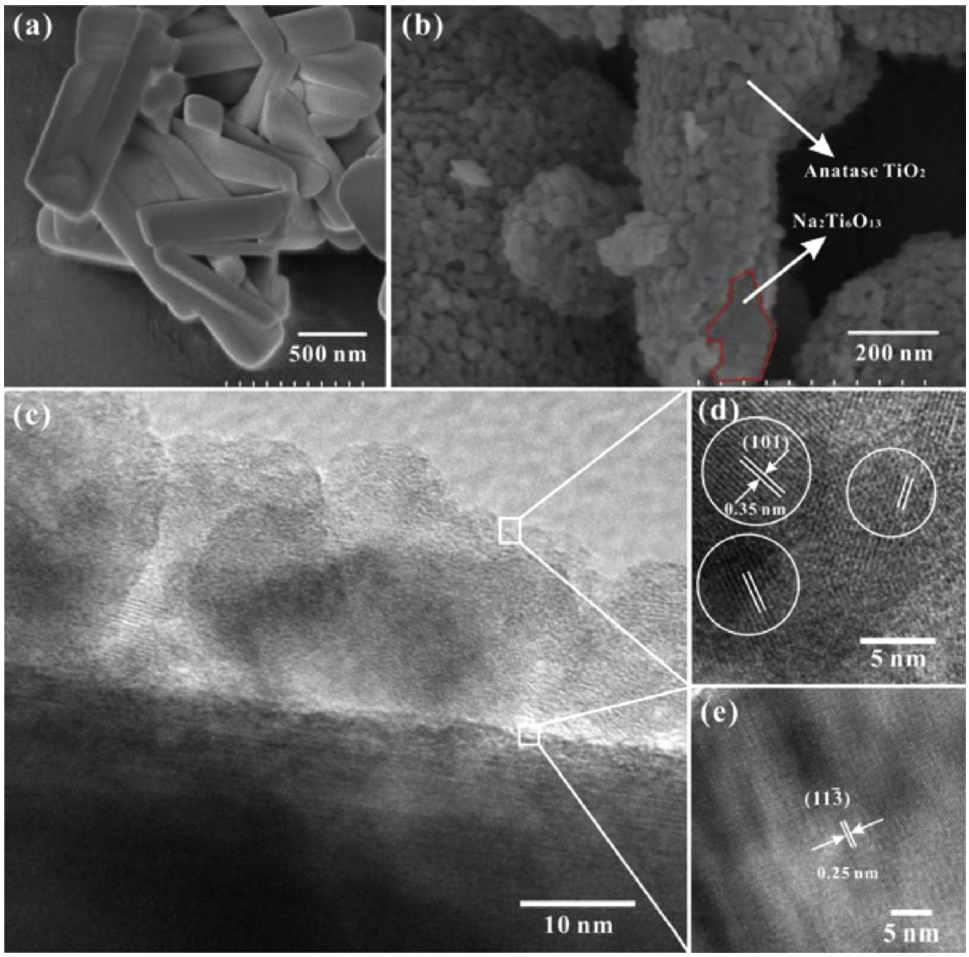

Fig. 3. EM images of $Na_2Ti_3O_7$ and N–TTO-6-2. (a) SEM of $Na_2Ti_3O_7$, (b) SEM of N–TTO-6-2, and (c–e) HRTEM of N–TTO-6-2.

presence of $\{11\bar{3}\}$ plane with a lattice spacing of 0.25 nm. In addition, the HRTEM image of N–TTO-6-2 also demonstrates the highly crystalline nature of both TiO_2 and $Na_2Ti_6O_{13}$ and a closely contacted interface between two components due to the common structural features of TiO_6 octahedra in anatase TiO_2 and $Na_2Ti_6O_{13}$.

As we known, anisotropically shaped particles, such as nanobelts, nanorods, and nanotubes have been found to have a lower recombination rate of electron–hole pairs [30]. Thus, the long anisotropically shaped titanate nanobelts in N–TTO-6-2 are expected to inherently promote the separation of electron–hole pairs and the transfer of charge carriers to different reaction sites for subsequent reactions. This may be due to the fact that nanobelts possess a higher charge carrier mobility and provide the pathway for transport of charge carriers throughout the longitudinal direction. On the other hand, it was reported that the anatase TiO_2 nanocrystals with the reductive {1 0 1} facets could be acted as a possible reservoir of the photogenerated electrons, yielding a highly reactive surface for the reduction of O_2–$O_2^{\bullet-}$ [30]. Thus, the charge separation was promoted and the recombination rate of electron–hole pairs was lowered, leading to an enhanced photocatalytic activity [31,42,43].

3.3. XPS studies

The chemical composition and states of atoms in the resulted composites were further determined by XPS and taking N–TTO-6-2 as an example. It can be seen from Fig. 4(a) that the sample consists of C, N, Ti, and O elements. The carbon peak is attributed to adventitious hydrocarbon from the XPS instrument. As shown in Fig. 4(b), the N 1s spectrum of N–TTO-6-2 can be fitted into two peaks. According to the previous reports, the peak with a lower binding energy at 397.9 eV is arisen from the substitution of nitrogen for oxygen in the form of O—Ti—N linkages due to N atoms being bonded to Ti atoms and replacing lattice oxygen atoms in TiO_2 [44,45]. The peak with a higher binding energy of 399.9 eV can be ascribed to oxidized states, such as Ti—O—N···Ti and Ti—N—O···Ti linkages [46–48]. This assignment assumes some type of interaction between nitrogen and oxygen to yield the peaks at ~400 eV [47,48]. The interstitial bonds of Ti—O—N···Ti and Ti—N—O···Ti show a higher binding energy than the substituted O—Ti—N bond, because the high electronegativity of O reduces the electron density on N [49]. Combined with EM results, it is reasonable to assume that N is mainly incorporated into TiO_2 as titanate core is fully covered with TiO_2 shell with a thickness of 15–20 nm and N doping proceeds from the exterior to the interior.

As shown in Fig. 4(c), in the case of N–TTO-6-2, two peaks at 458.0 and 463.8 eV could be attributed to the levels of Ti $2p_{3/2}$ and Ti $2p_{1/2}$ spin orbital splitting photoelectrons in the Ti^{4+} chemical state, respectively [49]. These two peaks are quite similar to those in TTO-6 and $Na_2Ti_3O_7$, and thus, can be assigned to the octahedrally coordinated Ti. In addition, there shows no shoulder at lower binding energies which are classically attributed to Ti^{3+} species due to oxygen vacancies, indicating the existence of only Ti^{4+} in N–TTO-6-2 [50,51]. As shown in Fig. 4(d), the O 1s spectrum can be evaluated by two peak fitting. The peak at a lower binding energy of 529.5 eV can be ascribed to lattice oxygen in composite, while the signal at 531.6 eV is associated with the oxynitride or adsorbed water [52].

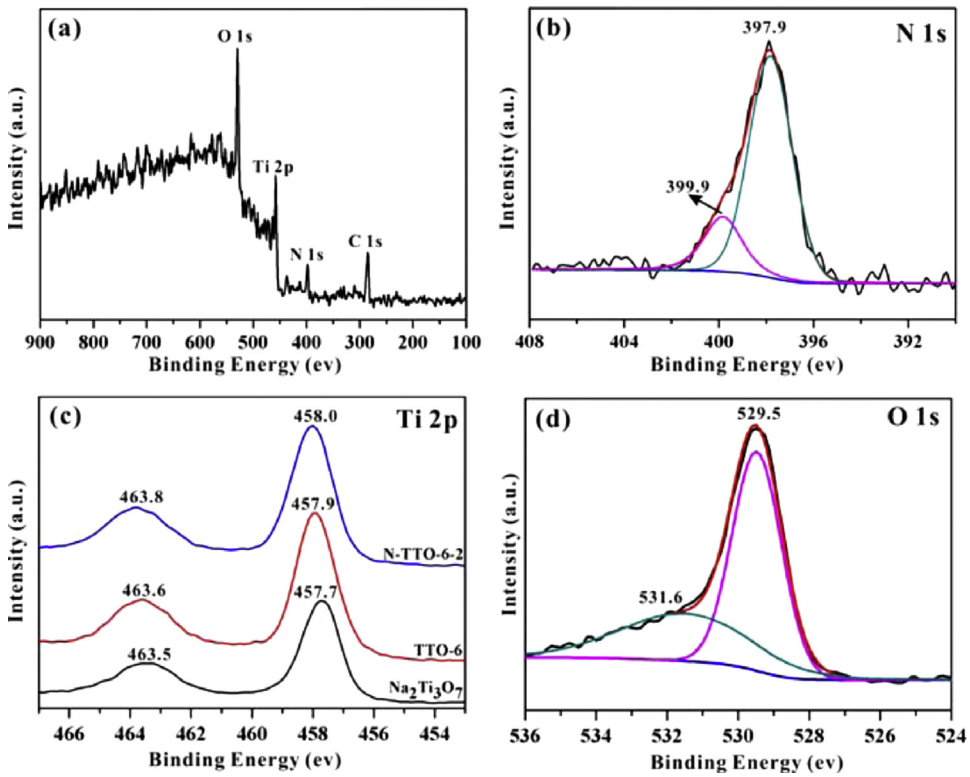

Fig. 4. XPS spectra of N–TTO-6-2 (a) a total spectrum, (b) N 1s spectrum, (c) Ti 2p spectrum, and (d) O 1s spectrum.

3.4. UV–vis diffuse reflectance spectra

Fig. 5(a) shows UV–vis diffuse reflectance spectra of $Na_2Ti_3O_7$, TTO-6, N–TiO_2, and N–TTO-6-2. Only an absorption band, which is attributed to the band-to-band transition, can be observed in the UV region for $Na_2Ti_3O_7$. After hybridizing titanate with TiO_2, the resulted TTO-6 shows a much stronger absorption in UV region. In addition, it can also be observed that the band gap energy of TTO-6 is shifted from 353 (ca. 3.51 eV) to ~385 nm (ca. 3.22 eV) according to the position of the absorption edge. Apart from the possible quantum size effect [53], this might be predominantly due to the formation of heterojunction between $Na_2Ti_6O_{13}$ (3.53 eV) and anatase TiO_2 (ca. 3.20 eV) as a result of the electronic coupling between two components within the closely contacted interface [9,33]. Furthermore, after N doping, the resulted N–TTO-6-2 shows a significant absorption tail in the visible region from 400 to 542 nm. Compared with N–TiO_2, N–TTO-6-2 has a more strong visible-light response although its absorption in UV region is relatively weaker, further confirming the formation of heterojunction between $Na_2Ti_6O_{13}$ and TiO_2. Moreover, the visible light response behavior after N doping was also clearly evidenced from the apparent color change of the resulting N–TTO-6-2 from white to yellow.

The absorption spectrum of N–TTO-6-2 may further provide some information about the band structure of the sample [54,55]. As shown in Fig. 5(a), it exhibits a two-step absorption edge. The first edge is related to the band structure of titanate while the second edge extended to the visible region can be attributed to the band created by N doping. An impurity energy level is formed within the band gap of the resulted nanohybrid due to N doping, resulting in the visible light absorption of N–TTO-6-2. Combined with XPS results, it is estimated that the induced sub-band gap excitation is attributed to an isolated N 2p state rather than the mixed states of N 2p and O 2p [25,55].

As shown in Fig. 5(b), the absorption in the visible light region of N–TTO-*x*-2 series composites is gradually enhanced with the loading amount of TiO_2 and reaches a maximum for sample N–TTO-6-2 with a TiO_2 loading amount of 45.9 wt%. Correspondingly, the energy gap (E_g) is decreased from 3.12 to 2.50 eV (see Table S1). However, a further increase of the loading amount of TiO_2 leads to an obvious decrease of the absorption in the visible light region and the increase of E_g. It indicates that an appropriate mass ratio of

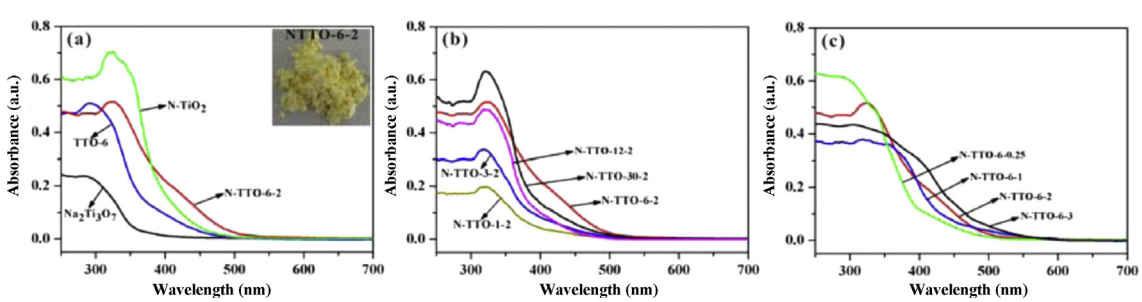

Fig. 5. Diffuse reflectance UV–vis spectra of (a) $Na_2Ti_3O_7$, TTO-6, N–TTO-6-2, and N–TiO_2 (inset is a photograph of N–TTO-6-2), (b) N–TTO-*x*-2 series composites with different loading amounts of TiO_2 (x = 1, 3, 6, 12, and 30), and (c) N–TTO-6-*y* series composites with different contents of doped N (y = 0.25, 1, 2, and 3).

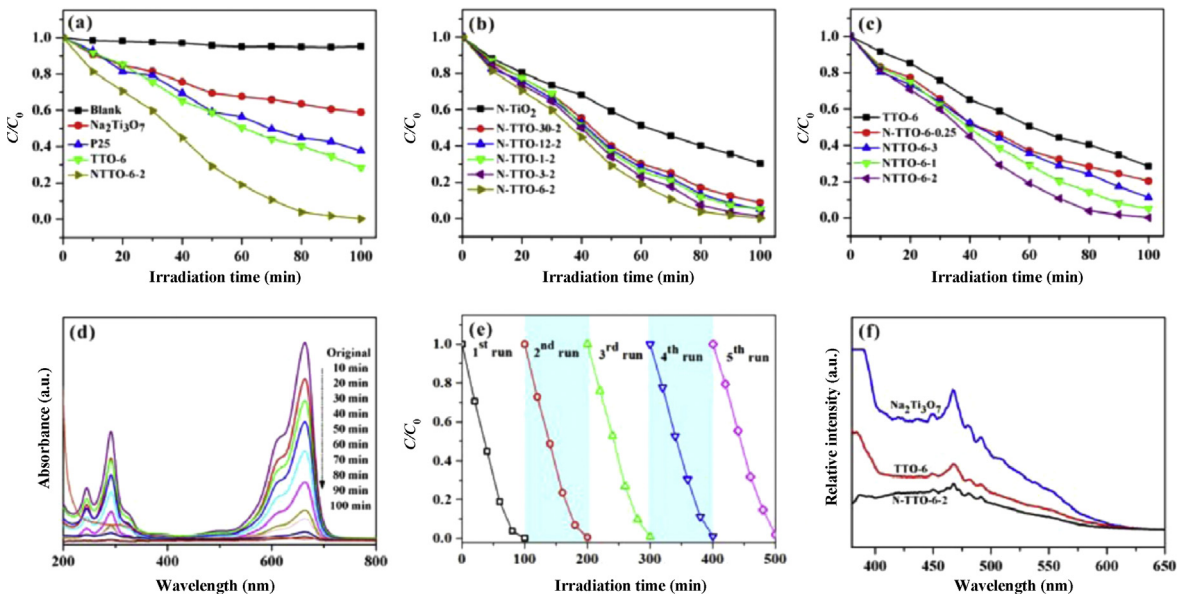

Fig. 6. (a–c) Visible light photocatalytic degradation rate of MB over different samples, (d–e) UV–vis spectra and photocatalytic stability of MB over N–TTO-6-2 under visible light irradiation, and (f) PL spectra of $Na_2Ti_3O_7$, TTO-6, and N–TTO-6-2 with an excitation wavelength of 325 nm.

TiO_2 and titanate is essential for the formation of heterojunction in the composite and thus, the absorption in the visible light region is greatly improved. On the other hand, as shown in Fig. 5(c), it is obvious that the absorption in the visible light region of N–TTO-6-*y* series composites with different contents of doped N is gradually strengthed with the content of doped N. Correspondingly, the energy gap (E_g) is decreased from 3.02 to 2.24 eV (see Table S2). It indicates that N doping under present conditions is successfully achieved and also there is a direct effect of the content of doped N on the visible region absorption.

Apparently, the nitrogen dopant greatly promoted the light harvesting ability [56,57]. Since there is no red shift of the band edge and negligible absorption above 600 nm, the enhanced response to visible light should be attributed to the localized states near the top of VB of anatase TiO_2 introduced by nitrogen dopant, rather than the generation of oxygen vacancies [58]. As the energy potentials of the CB and VB are −0.53 and 2.67 eV in anatase TiO_2 and the composite N–TTO-6-2 has a strong absorption below 495 nm (i.e., E_g = 2.50 eV), the highest potential of localized N 2p states introduced by N dopant in anatase TiO_2 can be calculated as ∼1.97 eV [33].

3.5. Visible light photocatalytic performance

Fig. 6(a) shows the photocatalytic activities of $Na_2Ti_3O_7$, TTO-6, and N–TTO-6-2 along with the commercial P25 under visible light irradiation. Firstly, MB solution was illuminated under visible light irradiation in the absence of photocatalyst and the result indicates that the degradation of MB is neglectable. There is a non-negligible reduction of MB in the presence of $Na_2Ti_3O_7$, which is essentially due to the self-photosensitized oxidation. Although $Na_2Ti_3O_7$ itself cannot be excited by visible light due to its large energy band gap, MB can absorb visible light and the redox potential of its lowest excited state (−0.71 eV) is more negative than the CB edge potential of $Na_2Ti_3O_7$ (−0.50 eV). Hence, the photogenerated electrons might be transferred from MB to $Na_2Ti_3O_7$ and thus, $Na_2Ti_3O_7$ shows a photocatalytic activity under visible light irradiation even though it has no light absorption in visible light region [59]. After hybridizing titanate with TiO_2, the resulted TTO-6 shows an enhanced photocatalytic activity than the pure $Na_2Ti_3O_7$ due to the formation of heterojunction and thus, the effective spatial separation of photogenerated electron–hole pairs [60]. By comparison, N–TTO-6-2 shows a further significantly enhanced photoactivity than TTO-6, indicating that N doping essentially tunes the electric structure of TTO-6 and thus, further effectively enhances the photocatalytic performance [61,62]. Combined with the results from UV–vis spectra, the observed photobleaching over N–TTO-6-2 under visible light irradiation should be mainly due to the oxidative photodegradation of dye molecules rather than self-photosensitized oxidation or other reasons. More importantly, compared with the commercial P25, N–TTO-6-2 shows an obviously enhanced photocatalytic performance with 99.2% MB photodegraded in 100 min.

As shown in Fig. 6(b), it can be observed that the photocatalytic activity of N–TTO-*x*-2 series samples with different loading amounts of TiO_2 first increases with the amount of TiO_2 and reaches a maximum with N–TTO-6-2. However, the activity decreases as the amount of TiO_2 is further decreased. It indicates that an appropriate mass ratio of TiO_2 and titanate is important for achieving an excellent activity. As mentioned above, an appropriate mass ratio of TiO_2 and titanate is essential for the formation of heterojunction between two components and thus, the enhancement of photocatalytic activity. Nevertheless, when there is an excess amount of TiO_2, the thickness of TiO_2 shell becomes too large that photogenerated electrons will not be so easy to be transferred from TiO_2 shell to titanate core across heterojunction, leading to the decrease of activity. In addition, all N–TTO-*x*-2 series samples have a much higher activity than N–TiO_2 due to the unique core–shell structure and synergistic effects of TiO_2 and titanate in the resulted composites.

Fig. 6(c) presents the photocatalytic activities of N–TTO-6-*y* series samples with different contents of doped N. For comparison, an undoped sample (TTO-6) is also included. All N-doped samples show an obviously enhanced activity than undoped TTO-6. In addition, it can also be found that the content of doped N has a great effect on the activity of the resulted composites. The photocatalytic activity is increased with the content of doped N and reaches the highest with N–TTO-6-2. However, an excess content of doped N leads to an obvious decrease of activity with N–TTO-6-3. The above phenomena can be explained as follows. First, as stated above, N doping could create a donor level above the original valence band of composites to increase the absorption intensity in the visible light region. Hence, huge numbers of electrons could be excited under visible region and thus, efficiently enhance the photocat-

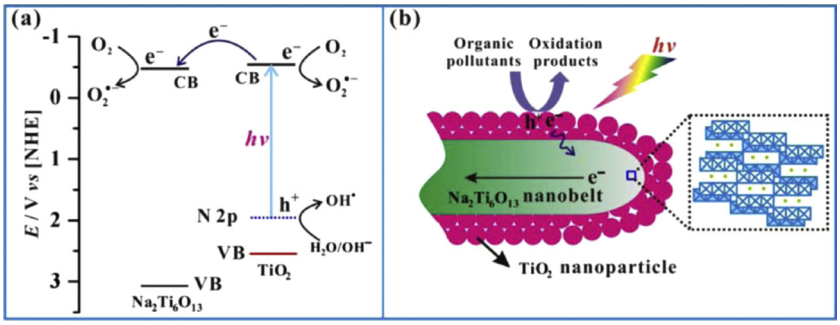

Fig. 7. (a) Energy levels of $Na_2Ti_6O_{13}$ and anatase TiO_2 in N–TTO-6-2 composite using normal hydrogen electrode (NHE) as reference at pH 7. The potential of CB band in TiO_2 was calculated from $E_{CB} = -0.12 - 0.059$ pH. (b) A schematic illustration of N–TTO-6-2 composite catalyst for the photodegradation of MB.

alytic performance. Second, as revealed by UV–vis spectra, the absorption in the visible light region is gradually strengthened and thus, more photogenerated electron–hole pairs are produced with the content of doped N. However, as the doping sites could also server as recombination centers for the photo-excited electrons and holes, an excess content of doped N is not favorable for achieving an excellent photocatalytic performance [55].

As show in Fig. 6(d), the rapid decrease in absorption intensity of all bands further shows that MB is efficiency degraded under visible light irradiation in the presence of N–TTO-6-2 composite. Moreover, even though the composite was reused five times, it still exhibited a high photoactivity (Fig. 6(e)). It indicates that N–TTO-6-2 has a high stability and does not photocorrode during the photocatalytic oxidation of the pollutant molecules.

As we know, the photocatalytic reaction depends largely upon the life of electron–hole pairs. Photoluminescence (PL) emission spectra can be used to study the separation of photogenerated charge carriers and thus, to understand the role of TiO_2 coupling and N doping in enhancing visible light activity for MB degradation [63]. Fig. 6(f) shows PL spectra of $Na_2Ti_3O_7$, TTO-6, and N–TTO-6-2 with an excitation wavelength of 325 nm. The main emission peak for $Na_2Ti_3O_7$ is centered at ~467 nm, which can be ascribed to the band gap recombination of electron–hole pairs [64]. The peak positions in TTO-6 and N–TTO-6-2 are similar to those in pure $Na_2Ti_3O_7$. It can be observed that TTO-6 has an obviously reduced PL intensity compared with $Na_2Ti_3O_7$, indicating that TTO-6 has a much lower recombination rate of photogenerated electron–hole pairs. It confirms the importance of heterojunction in hindering the recombination of electrons and holes.

On the other hand, compared with TTO-6, the PL of N–TTO-6-2 is further suppressed and shows a diminished intensity in the visible region. As shown in Fig. 1, during the preparation process of N–TTO-*x*-*y*, the urea was decomposed and thus, cyanic acid could be produced. The oxygen atoms in cyanic acid were then preferentially extracted by the composite to fill the surface oxygen vacancies and thus, the recombination center of photogenerated electrons and holes could be effectively decreased, giving rise to a much weaker intensity of PL emission in the visible region of the resulting sample N–TTO-6-2. Hence, the PL results imply that both TiO_2 hybridization and N doping can effectively accelerate the separation of charge carriers.

3.6. Photocatalytic mechanism

Based on the above Section 3, a possible mechanism for the photocatalytic degradation of MB over N–TTO-6-2 is proposed and schematically shown in Fig. 7. Under visible light irradiation, N-doped anatase in N–TTO-6-2 can be excited to generate electron–hole pairs. The generated electrons are excited from N 2p states to CB, leaving behind holes in the N 2p states. As the energy potentials of the CB and VB in $Na_2Ti_6O_{13}$ are −0.50 and 3.03 eV while those in N-doped anatase are −0.53 and 1.97 eV [33,65], accumulation of photogenerated electrons on TiO_2 will migrate from CB of TiO_2 to that of $Na_2Ti_6O_{13}$ due to the potential difference, leading to the improved utilization of charge carriers and ultimately the enhanced photodegradation rate of MB.

In the case of N–TTO-6-2, the absorption of a photon excites an electron to the CB (e_{CB}^-), generating a positive hole in the valence band (h_{VB}^+) (Eq. (1)). The photogenerated electrons in the CB are transferred to adsorbed oxygen molecules (O_2) on the surface of catalyst, acting as electron scavengers to produce superoxide anion radicals ($O_2^{\bullet-}$) (Eq. (2)). The resulted $O_2^{\bullet-}$ radicals then react with H^+ to generate hydroperoxyl radicals ($HO_2^\bullet$) and subsequently H_2O_2 as shown in (Eqs. (3)–(4)) [6,66]. H_2O_2 may further react with e_{CB}^- to form $^\bullet$OH radicals and hydroxyl anions (Eq. (5)), inhibiting the recombination of electron–hole pairs [66]. Meanwhile, the formed holes can react with OH^- group or H_2O molecules to produce $^\bullet$OH radicals (Eq. (6)) which are responsible for the degradation of organic pollutant (Eq. (7)). The possible photocatalytic reactions are proposed as follows:

$$\text{N–TTO-6-2} + h\nu \rightarrow e_{CB}^- + h_{VB}^+ (\text{chargecarriergeneration} \quad (1)$$

$$O_2 + e_{CB}^- \rightarrow O_2^{\bullet-} \quad (2)$$

$$H^+ + O_2^{\bullet-} \rightarrow HO_2^\bullet \quad (3)$$

$$HO_2^\bullet + H^+ + e^- \rightarrow H_2O_2 \quad (4)$$

$$H_2O_2 + e_{CB}^- \rightarrow {}^\bullet OH + OH^- \quad (5)$$

$$H_2O + h_{VB}^+ \rightarrow {}^\bullet OH + H^+ \quad (6)$$

$$MB + {}^\bullet OH \rightarrow \text{oxidationproducts} \quad (7)$$

4. Conclusions

Novel composites, N-doped $Na_2Ti_6O_{13}$@TiO_2 core–shell nanobelts, have been synthesized via a simple two-step route. Anatase TiO_2 nanoparticles with specifically exposed {1 0 1} facets were deposited on the external surface of $Na_2Ti_6O_{13}$, leading to the maximized interfacial contact between anatase TiO_2 and $Na_2Ti_6O_{13}$ due to common structural features of TiO_6 octahedra in two components. It was found that both the loading amount of TiO_2 and the content of doped N have a great effect on the physicochemical properties and photocatalytic activity of the resulted composites. The resulted composite displayed an excellent photocatalytic performance in degrading MB under visible light irradiation owing to the following reasons. Firstly, the nanobelts possessed a higher charge carrier mobility and provided the pathway for transport of charge carriers throughout the longitudinal direction to different reaction sites for subsequent reactions. Secondly, the exposed {1 0 1} anatase facets acted as a possible reservoir of the photogenerated electrons, yielding a

highly reactive surface for the reduction of O_2–$O_2^{\bullet-}$. Thirdly, the heterojunction structure achieved between $Na_2Ti_6O_{13}$ and anatase TiO_2 further greatly decreased the recombination probability of photogenerated electron–hole pairs and increased the lifetime of charge carries. Finally, the band gap became narrowed through nitrogen doping, and thus, the light response was expanded to the visible region. The present work may provide an insight for the fabrication of novel visible-light photocatalysts with an excellent performance.

Acknowledgements

The authors greatly appreciate the financial support of Specialized Research Fund for the Doctoral Program of Higher Education (SRFDP, 20130091110010), Natural Science Foundation of Jiangsu Province (BK2011438), National Science Fund for Talent Training in Basic Science (no. J1103310), National Basic Research Program (973 Project) (no. 2009CB623504) and the Modern Analysis Center of Nanjing University. This work was also supported by a Project Funded by the Priority Academic Program Development of Jiangsu Higher Education Institutions.

Appendix A. Supplementary data

Supplementary data associated with this article can be found, in the online version, at http://dx.doi.org/10.1016/j.apcatb.2015.01.026.

References

[1] X.B. Chen, S.H. Shen, L.J. Guo, S.S. Mao, Chem. Rev. 110 (2010) 6503–6570.
[2] C.C. Chen, W.H. Ma, J.C. Zhao, Chem. Soc. Rev. 39 (2010) 4206–4219.
[3] Y.P. Chen, C.L. Lu, L. Xu, Y. Ma, W.H. Hou, J.J. Zhu, CrystEngComm 12 (2010) 3740–3747.
[4] L. Xu, X.Y. Yang, Z. Zhai, W.H. Hou, CrystEngComm 13 (2011) 7267–7275.
[5] C.W. Tan, G.Q. Zhu, M. Hojamberdiev, K. Okada, J. Liang, X.C. Luo, P. Liu, Y. Liu, Appl. Catal. B: Environ. 152–153 (2014) 425–436.
[6] M. Pelaez, N.T. Nolan, S.C. Pillai, M.K. Seery, P. Falaras, A.G. Kontos, P.S.M. Dunlop, J.W.J. Hamilton, J.A. Byrne, K. O'Shea, M.H. Entezari, D.D. Dionysiou, Appl. Catal. B: Environ. 125 (2012) 331–349.
[7] A.L. Linsebigler, G.Q. Lu, J.T. Yates, Chem. Rev. 95 (1995) 735–758.
[8] A. Kubacka, M. Fernández-García, G. Colón, Chem. Rev. 112 (2011) 1555–1614.
[9] O. Vázquez-Cuchillo, R. Gómez, A. Cruz-López, L.M. Torres-Martínez, R. Zanella, F.J.A. Sandoval, K. Del Ángel-Sánchez, J. Photochem. Photobiol. A 266 (2013) 6–11.
[10] Y.C. Pu, Y.C. Chen, Y.J. Hsu, Appl. Catal. B: Environ. 97 (2010) 389–397.
[11] V. Rodríguez-González, M.A. Ruiz-Gómez, L.M. Torres-Martínez, R. Zanella, R. Gómez, Catal. Today 148 (2009) 109–114.
[12] M. Shirpour, J. Cabana, M. Doeff, Chem. Mater. 26 (2014) 2502–2512.
[13] A. Rudola, K. Saravanan, S. Devaraj, H. Gong, P. Balaya, Chem. Commun. 49 (2013) 7451–7453.
[14] Y.M. Wang, G.J. Du, H. Liu, D. Liu, S.B. Qin, N. Wang, C.G. Hu, X.T. Tao, J. Jiao, J.Y. Wang, Z.L. Wang, Adv. Funct. Mater. 18 (2008) 1131–1137.
[15] C.Y. Xu, J. Wu, P. Zhang, S.P. Hu, J.X. Cui, Z.Q. Wang, Y.D. Huang, L. Zhen, CrystEngComm 15 (2013) 3448–3454.
[16] Y. Inoue, T. Kubokawa, K. Sato, J. Phys. Chem. 95 (1991) 4059–4063.
[17] M. Kitano, M. Hara, J. Mater. Chem. 20 (2010) 627–641.
[18] A. Kudo, Y. Miseki, Chem. Soc. Rev. 38 (2009) 253–278.
[19] J.J. Guo, S.X. Ouyang, P. Li, Y.J. Zhang, T. Kako, J.H. Ye, Appl. Catal. B: Environ. 134–135 (2013) 286–292.
[20] T. Sano, N. Mera, Y. Kanai, C. Nishimoto, S. Tsutsui, T. Hirakawa, N. Negishi, Appl. Catal. B: Environ. 128 (2012) 77–83.
[21] X. Guo, H.J. Zhu, Q. Li, Appl. Catal. B: Environ. 160–161 (2014) 408–414.
[22] X.B. Chen, C. Burda, J. Am. Chem. Soc. 130 (2008) 5018–5019.
[23] V. Trevisan, A. Olivo, F. Pinna, M. Signoretto, F. Vindigni, G. Cerrato, C.L. Bianchi, Appl. Catal. B: Environ. 160–161 (2014) 152–160.
[24] Z. Zhai, X.Y. Yang, L. Xu, C.H. Hu, L.H. Zhang, W.H. Hou, Y.N. Fan, Nanoscale 4 (2012) 547–556.
[25] Z. Zhai, C.H. Hu, X.Y. Yang, L.H. Zhang, C. Liu, Y.N. Fan, W.H. Hou, J. Mater. Chem. 22 (2012) 19122–19131.
[26] Y. Liu, M.Y. Zhang, L. Li, X.T. Zhang, Appl. Catal. B: Environ. 160–161 (2014) 757–766.
[27] H.G. Yang, C.H. Sun, S.Z. Qiao, J. Zou, G. Liu, S.C. Smith, H.M. Cheng, G.Q. Lu, Nature 453 (2008) 638–641.
[28] H.G. Yang, G. Liu, S.Z. Qiao, C.H. Sun, Y.G. Jin, S.C. Smith, J. Zou, H.M. Cheng, G.Q. Lu, J. Am. Chem. Soc. 131 (2009) 4078–4083.
[29] J. Pan, G. Liu, G.Q. Lu, H.M. Cheng, Angew. Chem. Int. Ed. 50 (2011) 2133–2137.
[30] M. D'Arienzo, J. Carbajo, A. Bahamonde, M. Crippa, S. Polizzi, R. Scotti, L. Wahba, F. Morazzoni, J. Am. Chem. Soc. 133 (2011) 17652–17661.
[31] N.Q. Wu, J. Wang, D.N. Tafen, H. Wang, J.G. Zheng, J.P. Lewis, X.G. Liu, S.S. Leonard, A. Manivannan, J. Am. Chem. Soc. 132 (2010) 6679–6685.
[32] M.-V. Sofianou, N. Boukos, T. Vaimakis, C. Trapalis, Appl. Catal. B: Environ. 158–159 (2014) 91–95.
[33] Z. Xiong, X.S. Zhao, J. Am. Chem. Soc. 134 (2012) 5754–5757.
[34] H.Y. Zhu, Y. Lan, X.P. Gao, S.P. Ringer, Z.F. Zheng, D.Y. Song, J.C. Zhao, J. Am. Chem. Soc. 127 (2005) 6730–6736.
[35] H.Y. Zhu, X.P. Gao, Y. Lan, D.Y. Gao, Y.X. Song, J.C. Xi, J. Zhao, J. Am. Chem. Soc. 126 (2004) 8380–8381.
[36] S. Uchida, Y. Yamamoto, Y. Fujishiro, A. Watanabe, O. Ito, T. Sato, J. Chem. Soc. Faraday Trans. 93 (1997) 3229–3234.
[37] Z. Xiong, X.S. Zhao, J. Mater. Chem. A 1 (2013) 7738–7744.
[38] N. Miyamoto, K. Kuroda, M. Ogawa, J. Mater. Chem. 14 (2004) 165–170.
[39] Z. Zhai, Y.C. Huang, L. Xu, X.Y. Yang, C.H. Hu, L.H. Zhang, Y.N. Fan, W.H. Hou, Nano Res. 4 (2011) 635–647.
[40] J.K. Burdett, T. Hughbanks, G.J. Miller, J.W. Richardson, J.V. Smith, J. Am. Chem. Soc. 109 (1987) 3639–3646.
[41] H.W. Liu, D.J. Yang, Z.F. Zheng, X.B. Ke, E. Waclawik, H.Y. Zhu, R.L. Frost, J. Raman Spectrosc. 41 (2010) 1331–1337.
[42] G.K. Mor, O.K. Varghese, M. Paulose, K. Shankar, C.A. Grimes, Sol. Energy Mater. Sol. Cells 90 (2006) 2011–2075.
[43] L.Q. Ye, J.Y. Liu, Z. Jiang, T.Y. Peng, L. Zan, Nanoscale 5 (2013) 9391–9396.
[44] H.U. Lee, S.C. Lee, S. Choi, B. Son, H. Kim, S.M. Lee, H.J. Kim, J. Lee, J. Hazard. Mater. 258–259 (2013) 10–18.
[45] H.H. Ou, S.L. Lo, C.H. Liao, J. Phys. Chem. C 115 (2011) 4000–4007.
[46] H.X. Li, J.X. Li, Y.N. Huo, J. Phys. Chem. B 110 (2006) 1559–1565.
[47] X.X. Yang, C.D. Cao, L. Erickson, K. Hohn, R. Maghirang, K. Klabunde, Appl. Catal. B: Environ. 91 (2009) 657–662.
[48] S.H. Lee, E. Yamasue, K.N. Ishihara, H. Okumura, Appl. Catal. B: Environ. 93 (2010) 217–226.
[49] H.Q. Cao, B.J. Li, J.X. Zhang, F. Lian, X.H. Kong, M.Z. Qu, J. Mater. Chem. 22 (2012) 9759–9766.
[50] D.J.V. Pulsipher, I.T. Martin, E.R. Fisher, ACS Appl. Mater. Interfaces 2 (2010) 1743–1753.
[51] R. Schafranek, S. Payan, M. Maglione, A. Klein, Phys. Rev. B 77 (2008) 195310–195322.
[52] N.C. Saha, H.G. Tompkins, J. Appl. Phys. 72 (1992) 3072–3079.
[53] Z.J. Chen, B.Z. Lin, Y.L. Chen, K.Z. Zhang, B. Li, H. Zhu, J. Phys. Chem. Solids 71 (2010) 841–847.
[54] X.K. Li, N. Kikugawa, J.H. Ye, Chem. Eur. J. 15 (2009) 3538–3545.
[55] H. Irie, Y. Watanabe, K. Hashimoto, J. Phys. Chem. B 107 (2003) 5483–5486.
[56] Q.C. Xu, D.V. Wellia, R. Amal, D.W. Liao, S.C.J. Loo, T.T.Y. Tan, Nanoscale 2 (2010) 1122–1127.
[57] N.S. Chaudhari, S.S. Warule, S.A. Dhanmane, M.V. Kulkarni, M. Valant, B.B. Kale, Nanoscale 5 (2013) 9383–9390.
[58] Z.H. Lin, A. Orlov, R.M. Lambert, M.C. Payne, J. Phys. Chem. B 109 (2005) 20948–20952.
[59] H. Kisch, W. Macyk, ChemPhysChem 3 (2002) 399–400.
[60] B.H. Xu, B.Z. Lin, Q.Q. Wang, X.T. Pian, O. Zhang, L.M. Fu, Micropor. Mesopor. Mater. 147 (2011) 79–85.
[61] C.Y. Yang, Z. Wang, T.Q. Lin, H. Yin, X.J. Lü, D.Y. Wan, T. Xu, C. Zheng, J.H. Lin, F.Q. Huang, X.M. Xie, M.H. Jiang, J. Am. Chem. Soc. 135 (2013) 17831–17838.
[62] C.Q. Chen, P. Li, G.Z. Wang, Y. Yu, F.F. Duan, C.Y. Chen, W.G. Song, Y. Qin, M. Knez, Angew. Chem. Int. Ed. 52 (2013) 9196–9200.
[63] L.Q. Jing, Y.C. Qu, B.Q. Wang, S.D. Li, B.J. Jiang, L.B. Yang, W. Fu, H.G. Fu, J.Z. Sun, Sol. Energy Mater. Sol. Cells 90 (2006) 1773–1787.
[64] C. Liu, L. Wu, J. Chen, J.Y. Liang, C.S. Li, H.M. Ji, W.H. Hou, Phys. Chem. Chem. Phys. 16 (2014) 13409–13417.
[65] Y. Wang, H.M. Zhang, X.D. Yao, H.J. Zhao, ACS Appl. Mater. Interfaces 5 (2013) 1108–1112.
[66] M.N. Chong, B. Jin, C.W.K. Chow, C. Saint, Water Res. 44 (2010) 2997–3027.